Materials Today Bio 16 (2022) 100416

Contents lists available at ScienceDirect

Materials Today Bio

journal homepage: www.journals.elsevier.com/materials-today-bio

Tumor immunosuppressive microenvironment modulating hydrogels for second near-infrared photothermal-immunotherapy of cancer

Junjian Shen [a,1], Minghui Lin [b,1], Mengbin Ding [c], Ningyue Yu [c], Chun Yang [d], Deping Kong [b], Haitao Sun [d,*], Zongyu Xie [a,**]

[a] Department of Radiology, The First Affiliated Hospital of Bengbu Medical College, Bengbu, Anhui, 233000, PR China
[b] Institute of Translational Medicine, Shanghai General Hospital, Shanghai Jiao Tong University School of Medicine, 201620, Shanghai, PR China
[c] College of Chemistry, Chemical Engineering and Biotechnology, Donghua University, Shanghai, 201620, PR China
[d] Department of Radiology, Zhongshan Hospital, Fudan University, Shanghai Institute of Medical Imaging, Department of Cancer, Zhongshan Hospital, Fudan University, Shanghai, 200032, PR China

ARTICLE INFO

Keywords:
Hydrogels
Photothermal therapy
Immunotherapy
Metastasis
Breast cancer

ABSTRACT

Immunotherapy has recently been seen as a hopeful therapeutic device to inhibit tumor growth and metastasis, while the curative efficacy is limited by intrinsic immunosuppressive tumor microenvironment. Herein, we reported a tumor immunosuppressive microenvironment modulating hydrogel (TIMmH) platform to achieve second near-infrared (NIR-II) photothermal therapy (PTT) combined immunotherapy for durable inhibition of breast cancer. This TIMmH platform was synthesized through co-loading of NIR-II photothermal nanoagent and an immunoadjuvant cytosine-phosphateguanosine oligodeoxynucleotides (CpG ODNs) into the alginate hydrogel (ALG). Upon the administration of ALG into the tumor, the TIMmH was in situ formed via the coordination effect with Ca^{2+}, locally encapsulating the semiconducting polymer nanoparticles ($SP_{II}N$) and CpG in the colloid, achieving to prolong the accumulation time and prevent the premature damage and release of immunotherapeutic agents. Upon 1064-nm photoirradiation, the $TIMmH_{SD}$ was able to elevate the intratumoral temperature for the ablation of tumors, which could induce the apoptosis of tumor cells and achieve thermal immune activation by regulating of an immunosuppressive microenvironment. The TIMmH-mediated combined treatment effectively suppressed the growths of breast cancers, and even acquired a sustained inhibition of the lung metastasis. This study provides a novel tumor immunosuppressive microenvironment modulating hydrogel platform with NIR-II photoexcited capacity for the safe, effective and durable lung metastasis-inhibiting breast cancer treatment.

1. Introduction

Immunotherapy that enables a boost of the immune system to combat malignancies is considered as a promising tumor therapy in clinic [1,2]. Distinguish from common therapy strategies such as surgery, chemo- or radio-therapy that mainly focus on the primary lesions, immunotherapy is not only capable of confronting malignancies, but also preventing tumor recurrence and distant metastasis [3–5]. Among various immune therapeutic strategies, cancer vaccines [6,7], immune checkpoint blockade [8,9], and adoptive T cell therapy [10] are commonly used therapeutic approaches. Unfortunately, only a small part of patients is suitable and sensitive to the immune curative agents, which may be caused by various reasons, such as the barrier of tumor immunosuppressive microenvironment [11,12], severe immune-related adverse events (irAEs) [13,14], inefficient immune cell infiltration [15], etc.

CpG, as an immunoregulatory nucleic acid, is considered as the critical adjuvant in inducing cancer immune response and fighting tumors [16–18]. The CpG ODNs enable the excretion of interferon-α (IFN-α) via the identification of Toll-like receptor 9 in the early endosomes [19]. Then, in late endosomes, these CpG ODNs recognized by TLR molecules can promote the maturation of the antigen-presenting cells and the activation of innate immune cells, possessing the effective immunostimulatory effect to fight cancer [20–22]. Additionally, in static early endosomal, CpG-ODNs combined with heat shock protein 90 possess a

* Corresponding author.
** Corresponding author.
E-mail addresses: sht1720@163.com (H. Sun), zongyuxie@sina.com (Z. Xie).
[1] Junjian Shen and Minghui Lin contributed equally to this work.

https://doi.org/10.1016/j.mtbio.2022.100416
Received 6 April 2022; Received in revised form 14 August 2022; Accepted 30 August 2022
Available online xxxx

robust potent to stimulate secretion of IFN-α from conventional Dendritic Cells (DCs) [23,24]. Nevertheless, the effective immune stimulation of CpG-ODNs is often limited, which mainly caused by low cellular uptake, easy degradation and damage, insufficient content in tumor area, and short residence time in lysosome [25,26]. Although immunoadjuvant carriers have been discovered for effective transportation of CpG ODNs, the immune activation effects are still unsatisfactory result in the insufficient local content and short time of existence in lysosomes [27,28]. On the other hand, the systemic administration of immunotherapeutic agents was not only inefficient uptake, but more likely to induce the immune-related adverse effects [29]. Thus, more effective strategies for transportation of the CpG are urgently need to be developed. As for tumors in the superficial organs, injectable hydrogels in situ may be the promising strategy for transportation of CpG, not only leading to higher content at tumor site than the systemic approach and prolongation of the retention time of immunodrugs, but also the prevention of rapid degradation [30]. Especially, intelligent injectable hydrogels endowed with property of activatable phase transition in special tumor microenvironment (TEM) including temperature, pH, calcium ion concentration, etc., have been widely considered as promising nanoplatform for durable drug release [31]. For example, owing to the good biocompatibility, hypotoxicity, easy modification, and well Ca^{2+}-responsive gelatinization, alginate hydrogel (ALG) has been widely applied in the area of biomedicines. ALG can be constructed through various cross-linking methods, and its good biocompatibility allows comprehensive applications in the biological field, such as wound healing, delivery of bioactive small molecule drugs, etc [32]. To be noted, the various drugs loaded in ALG were not only delivered into body through injection or oral administration but also released in a controllable manner, implying its superior bio-hydrogel carrier performance.

Photothermal therapy (PTT) that enables the production of heat for tumor thermal ablation via utilizing nanoagents is considered the promising therapeutic strategy for combating malignant tumors owing to the merits of low invasiveness, easy maneuverability, and high temporal-spatial resolution [33]. Although near-infrared (NIR) light in the first NIR window (NIR-I, range from 650 to 950 nm) is often used to mediate PTT, the laser in the bio-window has several inherent defects, including low penetration and limited maximum permissible exposure for skin [34]. However, the light in the second window (NIR-II, range from 1000 to 1300 nm) has recently been conducted for more effective tumor thermal ablation owing to the merits of deeper penetration depth and lower photo-toxicity [35,36]. Except for direct ablation of lesions, the PTT-mediated thermal energy can be used to synergize various curative modalities, such as chemotherapy [37,38], immunotherapy [39], photodynamic therapy (PDT) [40], etc., for obtaining more improved curative outcomes. Interestingly, PTT-produced thermal effects are reported to induce immune responses through different modes, such as activation of immunogenic cell death (ICD) and secretion of immunostimulatory agents, which may produce the synergized effect to the immunoadjuvants CpG [29]. In previous studies, NIR-I PTT has been performed to synergized with the CpG [41]. For example, Zheng's team has reported two-dimensional palladium nanosheets, served as vehicle of CpG, mediated the NIR-I PTT (808 nm), synergized with CpG-based immunotherapy, showing highly efficient tumor growth [42]. Unsatisfactory, low laser penetration depth and insufficient local content of CpG are still not be solved in their study, leading to the incomplete immune-activation effect.

As such, in present study, we fabricated a tumor immunosuppressive microenvironment modulating hydrogel platform and verified its function for NIR-II PTT-synergized immunotherapy to suppress durable breast cancer metastasis. This TIMmH platform was developed through the co-loading of $SP_{II}N$, as a NIR-II nanoagent, and CpG ODNs, an immunoadjuvant, into the alginate hydrogel. Due to the excellent optical properties, well biocompatibility as well as easy modification, semiconducting polymers (SPs) and their derivatives have been widely applied into the biomedical field, such as imaging of bio-tissues, tumor biomarkers, tumor phototherapy, regulation of biomedical events [43]. Especially, such SPs with well absorption in the NIR-II region showed excellent photothermal conversion efficiency, often serving as the photothermal agent to perform NIR-II PTT for inhibiting tumor growth. More importantly, in comparison with the NIR-I SPs, such NIR-II SPs can produce a better PTT effect in the deep tumor tissue for tumor inhibition growth, which may lead to more potent immunogenic cell death of tumor cells [44]. The $SP_{II}N$ are developed through the nanoprecipitation of amphiphilic polymers and SP_{II}, possessing better hydrophilicity and biocompatibility to facilitate cellular uptake [45]. On the other hand, to boost the accumulation and stability, ALG-based hydrogels possessing prominent in situ gelation quality and well biocompatibility have been used as a nano-vector [46]. Precursor mixtures by simply melding ALG with $SP_{II}N$ and CpG were locally administrated in a less invasive manner for acquiring the satisfactory drug accumulation in tumors (Fig. 1a). Upon the administration of ALG into the tumor site, the TIMmH was in situ formed by the coordination effect with Ca^{2+} in tumor environment, which locally encapsulated $SP_{II}N$ and CpG in the colloid, achieving to prolong the accumulation time of drugs and prevent the premature damage and release of CpG. Upon NIR-II photoexcitation, $SP_{II}N$ enabled the local elevation of the temperature for the ablation of tumors, which could efficiently induce apoptosis of cells and trigger initiation of ICD and maturation of DCs (Fig. 1b). Then, the synergistic effect of PTT the CpG ODNs-based immune effects modulated tumor immunosuppressive microenvironment from “cold” to “hot” immune state. As expected, the developed TIMmH nanoplatform not only served as the excellent vector of immunoadjuvants, but also effectively acquired the thermal immune activation through the modulation of tumor immunosuppressive microenvironment, ultimately obtaining the durable suppression of the breast tumor and metastasis.

2. Materials and methods

2.1. Materials

Anhydrous $CaCl_2$ and ALG were obtained from Aladdin Reagent Co. Ltd. (China). Bovine serum albumin (BSA) and Plorunic-F127 (F127) was obtained from Sigma-Aldrich (St. Louis, MO). CpG 1826 (5′-TCC ATG ACG TTC CTG ACG TT-3′) was purchased from the Sangon Biotechnology Co., Ltd. BV605-anti-mouse CD11c (Biolegend, Clone: N418, Catalog No. 117306), and CD8-PE (Biolegend, Clone: 53-5.8, Catalog No. 140408) were obtained from Biolegend (San Diego, USA). Anti-calreticulin antibody (Catalog No. ab227444), recombinant anti-HMGB1 antibody (Catalog No. ab79823) were obtained from Abcam. Ultrapure water used was obtained using a water purification system (PALL Cascada, MI).

2.2. Synthesis of $SP_{II}N$

SP_{II} (5 mg) and F127 (400 mg) were dissolved in 3 mL THF, and then sonicated for 5 min. Next, the above solution was simultaneously injected into 10 mL mixture solution of THF and ultrapure water (v_{THF}/v_{water} = 1:9) under the ultrasound condition for 30 min. The excess unreacted solvent of the mixed liquor was removed via a rotary evaporator. Then, the products were compassed by a polycarbonate membrane (220 nm). Finally, the obtained F127-SP_{II} were purified through ultrafiltration (3000 rpm, 15 min) using ultrafiltration device (50 KD) for three times at the centrifugal.

2.3. Synthesis of $TIMmH_{SD}$ hydrogels

To synthesize the TIMmH, ALG (100 mg) and CpG (1 mg/mL) were co-mixed in 10 mL PBS, which was then blended with $SP_{II}N$ (1 mg/mL). Next, the obtained mixed solution was slowly injected into 10 mL Ca^{2+} solution (1.8 mM) in a glass bottle, forming the final $TIMmH_{SD}$ ($SP_{II}N$–CpG@ALG hydrogel). The $TIMmH_S$ hydrogel ($SP_{II}N$@ALG hydrogel) as the control group was synthesized in the same way.

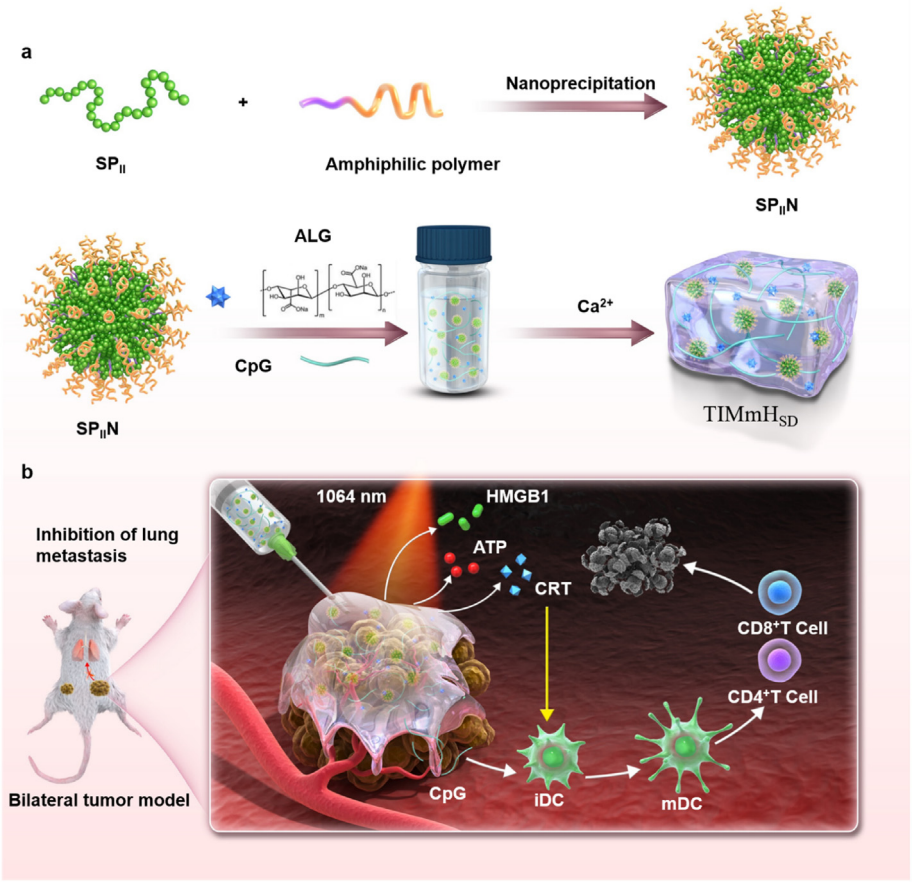

Fig. 1. Schematic diagram for injectable hydrogel preparation process $TIMmH_{SD}$.(a) and the mechanism of TIMmH-mediated thermal immunotherapy (b).

2.4. Characterization techniques

Dynamic light scattering and zeta potential of the $SP_{II}N$ was measured by using Zetasizer Nanoseries. The measurement of the UV–vis–NIR absorption spectra was performed via an UV-3600 spectrometer. The morphology of the prepared hydrogel was observed using a SEM (SU8010, HITACHI). The temperature and thermal images were measured using a thermo-camera (Fotric 220s camera). The fluorescence photos were recorded using an inverted fluorescence microscope (Leica DMi8, Germany). CytoFLEX flow cytometer (Beckman Coulter, USA) was used for the flow cytometry analysis.

2.5. Characterization of $TIMmH_{SD}$ hydrogels

500 μL of ALG (10 mg/mL) and 500 μL $SP_{II}N$ (1 mg/mL) solution and CpG (1 mg/mL) were added into Ca^{2+} solution (1.8 mM). Free $SP_{II}N$ without alginate was also used for comparison. Photographs at different times were taken after injection. 500 μL of ALG (10 mg/mL) mixed with $SP_{II}N$ (1 mg/mL) and CpG (1 mg/mL) was injected into 10 mL of Ca^{2+} solution in a bottle and then was shook for 24 h at 37 °C. The appearance changes of the $SP_{II}N$ in the Ca^{2+} solution was monitored, and the absorbance of the collected supernatant was assessed using a spectrophotometer to verify drug release. The rheological properties of ALG hydrogels and $TIMmH_{SD}$ hydrogels were tested via rheometer (Thermo HAAKE MARS 60).

2.6. Photothermal effect evaluation

Briefly, ALG (100 μL, 5 mg/mL), $SP_{II}N$ (100 μL, 100 μg/mL), $TIMmH_S$ (100 μL, $[SP_{II}N] = 100$ μg/mL, $[CpG] = 20$ μg/mL), and $TIMmH_{SD}$ (100 μL, $[SP_{II}N] = 100$ μg/mL, $[ALG] = 5$ mg/mL, CpG concentration = 20 μg/mL) solutions were illuminated using a 1064 nm laser (1 W/cm^2, 5 min), and the corresponding temperatures were recorded via a Fotric 220s photothermal camera. In addition, the photothermal ability of $TIMmH_{SD}$ at the different $SP_{II}N$ concentrations of (0, 12.5, 25, 50, 100 μg/mL) were further assessed, and the corresponding temperatures were also recorded at the same time. To compare the thermal ability of $TIMmH_S$ and $TIMmH_{SD}$ hydrogel at a certain concentration, the samples were exposed at a 1064 nm laser (1 W/cm^2, 5 min), and the temperatures were recorded every 60 s. The photothermal stabilities of both hydrogels were also evaluated. In brief, the hydrogel was exposed under the 1064 nm laser until it increased to maximum temperature. Then, the light was turns off until the temperature of the hydrogel decreased to near start temperature. Such turn on/off process was performed for five cycles. Corresponding temperatures were also recorded every 60 s.

2.7. In vitro cytotoxicity assay

The 4T1 cells were hatched in 96-well plates at a density of 1×10^4 cells each well for one day. Then, the cells were cultured with PBS (control), $TIMmH_S$, and $TIMmH_{SD}$ ($[SP_{II}N] = 0$, 12.5, 25, 50, 100 μg/mL) for one day. Finally, the CCK-8 was performed to assess the viability.

2.8. In vitro treatment effect

To measure the therapeutic effect of the hydrogel upon the photoirradiation, the cells were cultured with $TIMmH_S$ and $TIMmH_{SD}$ hydrogel at the $SP_{II}N$ concentrations of 0, 12.5, 25, 50, 100 μg/mL for 12 h. Then,

the cells in each well were irradiated with 1064 nm laser at a density of 1 W/cm^2 for 5 min and subsequently cultured for another 12 h. The CCK-8 kits was conducted for evaluating the viability.

2.9. The ICD in vitro

To verify the ICD in vitro, adenosine triphosphate (ATP), calreticulin(CRT) and high mobility group box 1 protein (HMGB1) as biomarkers of ICD were analyzed through different measurements. The ATP level was evaluated via ATP kit upon the manufacture protocols. In brief, 4T1 cells were cultivated for 24-well plates (10×10^4 cells/well) for 24 h. Then, the cells were treated with PBS, TIMmH$_S$, TIMmH$_{SD}$ ([SP$_{II}$N] = 100 μg/mL, [ALG] = 5 mg/mL, [CpG] = 20 μg/mL) for 6 h. In addition, the treated cells were irradiated without or with 1064 nm laser at a density of 1 W/cm^2 for 5 min and were cultured for another 6 h. Finally, the levels of ATP were detected by a luminometer. To explore the CRT, the 4T1 cells were seeded at 6-well plates (3×10^5 cells/well) for 24 h. Then, the cells were treated with PBS, TIMmH$_S$, TIMmH$_{SD}$ for 8 h. In addition, the treated cells were irradiated without or with 1064 nm laser (1 W/cm^2) for 5 min and then cultured for another 12 h. Each wall was washed two times with PBS, and the cells were digested by trypsin. Then, the treated cells were put on the centrifugal (1000 rpm, 5 min), subsequently the cells on the bottom were collected and were put into −80 °C to store. Finally, the levels of CRT were measured by western blot analysis. To explore the release of HMGB1, the 4T1 cells were cultivated at 12-well plates at a density of 20×10^4 cells each well for 24 h. Then, the cells were treated with PBS, TIMmH$_S$, TIMmH$_{SD}$ for 8 h. In addition, the treated cells were irradiated without or with 1064 nm laser (1 W/cm^2, 5 min) and were cultured for another 3 h, then the materials were removed and the cells were infiltrated with PBS for 3 min and were washed 3 times. Subsequently, the cells were fixed with 4% paraformaldehyde for 15 min, similarly, the 4% paraformaldehyde was removed and the cells were rinsed 3 times. Then, the cells were treated by rupture in liquid for 30 min. Next, the cells were closed with 10% BSA for 30 min. The cells were stained with HMGB1 of primary antibodies for 1 h at 37 °C, then the antibodies were removed and the cells were infiltrated with PBS for 3min and were washed 3 times. Then, the cells were stained using the second antibodies for 1 h at 37 °C, and the antibodies were removed and the cells were infiltrated with PBS for 3 min and were washed 3 times. Finally, the cells were co-cultured with DAPI for 5 min, and then the DAPI were washed with PBS and a small amount of PBS was added. The treated cells were assessed by inverted fluorescence microscope.

2.10. The tumor model establishment

The animal experiments in this study approved by the Ethical Committee of the First Affiliated Hospital of Bengbu Medical College (2021-303). All BALB/c mice (4 weeks old) in our study were obtained from SLAC Laboratory Animal Co., Ltd. In brief, the 4T1 cells were subcutaneously injected into the right flank of the mice. When the tumors volume in the right flank reached for 100 mm^3 for cancer treatment, the other tumors in the left flank were established using the above method for simulating distant tumor model.

2.11. The thermal imaging in vivo

4T1 tumor-bearing mice (tumor volume = 100^3) were locally administrated with PBS, TIMmH$_S$, TIMmH$_{SD}$ (20 μL, [SP$_{II}$N] = 100 μg/mL, [ALG] = 5 mg/mL, [CpG] = 20 μg/mL), respectively. After 2 h, the primary tumors of 4T1 tumor-bearing mice were illuminated with 1064 nm laser (1 W/cm^2, 5 min). The corresponding temperature of each tumor of mice was measured via a photothermal camera.

2.12. In vivo synergistic cancer therapy

The 4T1 tumor-bearing BALB/c mice were randomly divided into six groups (n = 5) as follows: PBS, PBS + laser, TIMmH$_S$, TIMmH$_S$ + laser, TIMmH$_{SD}$, TIMmH$_{SD}$ + laser group. The PBS, TIMmH$_S$ or TIMmH$_{SD}$ (20 μL, [SP$_{II}$N] = 100 μg/mL, [ALG] = 5 mg/mL, [CpG] = 20 μg/mL) were locally injected into the primary tumors of each group. Before treatment, the tumor volumes of each mouse were measured as initial tumor volumes. After 2 h, the primary tumors of each mouse were exposed at a 1064 nm laser (1 W/cm^2, 5 min). After that, the tumor sizes of tumors were measured every 2 d for 20 d by a caliper, and the corresponding tumor volumes were calculated as follows: volume (V) = (tumor length) × (tumor width)^2/2. Relative tumor volume was measured as V/V$_0$ (V$_0$ was the initial tumor volume). At the same time, the body weights of mice were measured every two days. After first photoexcitation for 24 h, the primary tumors of each group were extracted for H&E staining, TUNEL, and Ki-67 indexes to assess the therapeutic effect. Then, after treatment for 20 days, the tumors of mice were collected and weighted to measure tumor inhibition ratios. In addition, survival curves of all groups were also depicted after treatment. In order to assess the toxicity of nanoparticles, the corresponding major organs (heart, liver, spleen, kidney) were collected for H&E staining.

2.13. Inhibition of metastasis evaluation in vivo

Similar to the experimental procedure in the assessment of primary tumor growth, the distant tumors were measured and analyzed as described above. In addition, the lung metastatic tumors in mice were simultaneously for further assessing the anti-metastasis efficiency. In brief, the lung tissue of mice (n = 3) was extracted at 30 days, and the numbers of metastatic nodules were counted. Then, the lung metastatic tumors were stained for obtaining H&E images.

2.14. The evaluation of ICD and serum cytokine levels in vivo

In the aspect of ICD, the HMGB1 and CRT were respectively assessed. In brief, 4T1 tumor-bearing BALB/c mice were randomly divided into six groups as described above. The mice were locally administrated with 20 μL of PBS, TIMmH$_S$ and TIMmH$_{SD}$ ([SP$_{II}$N] = 100 μg/mL, [ALG] = 5 mg/mL, [CpG] = 20 μg/mL). After 24 h after photoexcitation (1064 nm, 1 W/cm^2, 5 min), the mice were sacrificed, and the tumors were obtained and respectively stained with anti-calreticulin antibody and recombinant anti-HMGB1 antibody. The corresponding fluorescence intensities in immunofluorescence staining were respectively measured and presented using a software Image J. As for evaluating the levels of different serum cytokines, on day 3 after treatments, the murine serum was extracted from mice in each group (n = 3). Then, each blood sample was measured using an ELISA kit to calculate the levels of serum interleukin-6 (IL-6), tumor necrosis factor-α (TNF-α), and interferon-γ (IFN-γ).

2.15. The evaluation of mature DCs in vivo

To assess the evaluation of mature DCs, the 4T1 tumor-bearing BALB/c mice were randomly divided into six groups as described above. After 2 h of post-injection, the primary tumors were exposed without or with 1064 nm laser (1 W/cm^2) for 5 min. On day 3 after treatments, the tumor-draining lymph nodes of the mice were extracted and stained with fluorophore-conjugated CD45-BV605, CD11c-FITC, CD80-PE, and CD86-APC antibodies according to the previous protocols. Finally, the samples in each mouse were evaluated by a flow cytometer.

2.16. Evaluation of T lymphocytes in vivo

To assess the evaluation of intratumoral T lymphocytes, the mice were divided into six groups (n = 3) as PBS, TIMmH$_S$ and TIMmH$_{SD}$ ([SP$_{II}$N] = 100 μg/mL, [ALG] = 5 mg/mL, [CpG] = 20 μg/mL). After local injection for 2 h, primary tumors in each group were exposed with or without a 1064 nm laser. At day 10, the distant tumors were extracted and prepared into single cell suspension. To investigate intratumoral

$CD8^+$ ($CD3^+CD8^+$) and $CD4^+$ ($CD3^+CD4^+$), all samples were stained with corresponding antibodies in line with the previous protocols, and analyzed.

2.17. The evaluation of biosafety in vivo

At the end of treatment, major organs (heart, liver, spleen, kidney) were extracted from mice in each group. All tissues were stained by H&E to observe the biosafety of nanoparticles.

2.18. Statistical analysis

The results were shown as mean ± standard deviation (SD). One-way ANOVA analysis are used to analyze statistical difference among different groups. The statistical differences were presented according to the p values and represented as follows: (*) for $p < 0.05$, (**) for $p < 0.01$, and (***) for $p < 0.001$.

3. Results and discussion

3.1. Characterization of $TIMmH_{SD}$ hydrogels

The $SP_{II}N$ are constructed amphiphilic polymers and SP_{II} via a nanoprecipitation method. In brief, SP_{II} and F127 were dissolved in THF, and then sonicated for 5 min. Next, the above solution was simultaneously injected into 10 mL mixture solution of THF and ultrapure water (v_{THF}/v_{water} = 1:9) under the ultrasound condition for 30 min. Finally, the $SP_{II}N$ were prepared. The hydrodynamic diameter of $SP_{II}N$ were measured to be 78.8 nm (Fig. S1). To assess the surface charge of prepared nanoparticles, The ζ-potential was measured to be −9.04 mV (Fig. S2). Subsequently, $SP_{II}N$ and CpG were co-loaded in ALG as the hydrogel matrix to form $TIMmH_{SD}$ through the coordination of calcium ion. To depict the morphology of $TIMmH_{SD}$, the SEM photos clearly represented that the nanoparticles gathering on the surface of hydrogel, indicating the ALG cross-linked by Ca^{2+} effectively enabled the immobilization of CpG and $SP_{II}N$ (Fig. 2a). Moreover, the UV–vis absorption spectra were listed. The ALG showed almost no absorption, whereas CpG owned a strong absorption at 263 nm. In contrast, the absorption of $SP_{II}N$ had an obvious peak at 1000–1100 nm, implying its well photothermal transversion capacity at NIR-II biowindow. The absorption spectrum of $TIMmH_{SD}$ had the similar characteristic peak of $SP_{II}N$ and CpG, proving the successful construction of $TIMmH_{SD}$ (Fig. 2b). The absorbance of $SP_{II}N$ with different concentrations ([$SP_{II}N$] = 6.25, 12.5, 25, 50, 100 μg/mL) gradually increased with the elevation of concentration (Fig. S3). To further verify the gel characteristic of TIMmH, the $SP_{II}N$ solutions were injected into Ca^{2+} solution without or with ALG (5 mg/mL), $TIMmH_S$ rapidly gelled after being injected with a syringe. After 2 h, the mixture liquid was observed to be a gel. While the alone $SP_{II}N$ dispersed in Ca^{2+} solution (Fig. 2d). After 24 h of shaking, the color of the supernatant was deepened, indicating that the contents of the developed hydrogel can be gradually released. In addition, rheological properties test indicated that the shear viscosity decreased with the rise of the shear rate, representing the satisfactory injectability of the developed hydrogel in this study (Fig. S4). To further quantitatively verify the slowly release performance of hydrogel, the UV–vis absorptions of CpG and $SP_{II}N$ in the supernatant liquid was further measured at different time points (Fig. 2c). Fig. 2e represented that a little drug release was observed at the first 6 h, while the released contents of drugs were could be gradually and measured as time extends, and the cumulative releases of CpG drug were measured to 67% after 24 h of shaking.

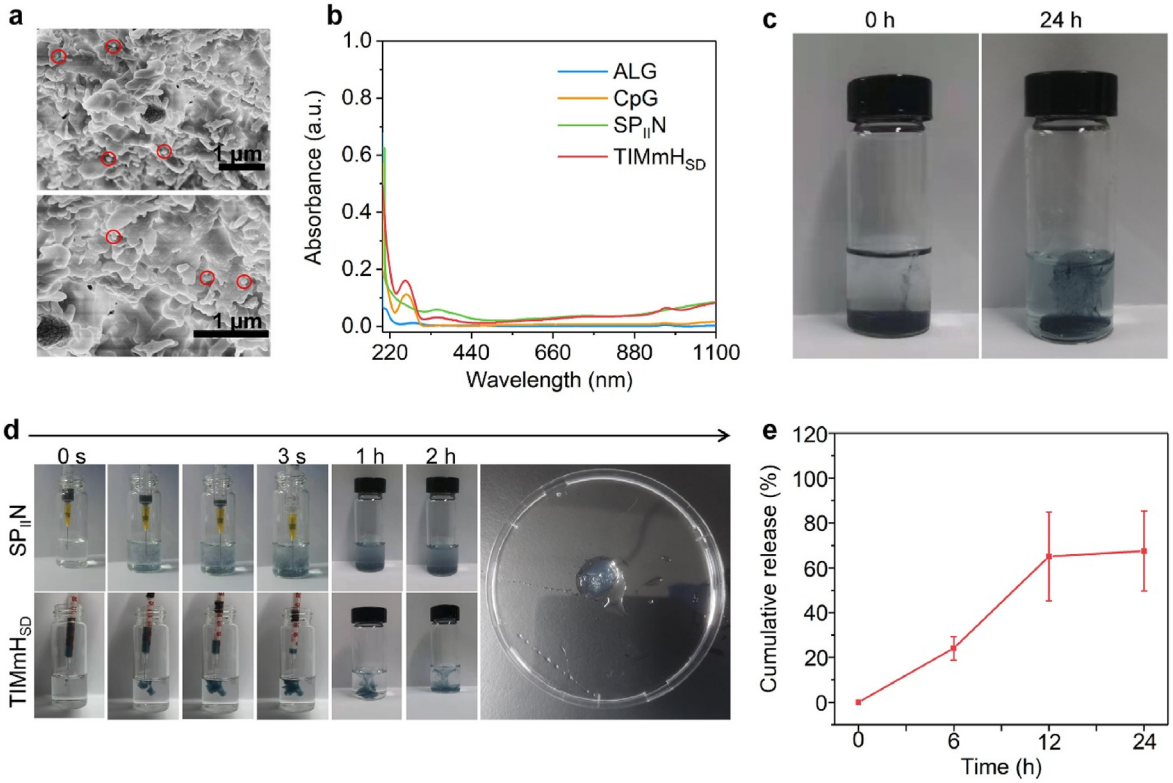

Fig. 2. Characterization of hydrogels. (a) The SEM images of $TIMmH_{SD}$ hydrogel and the high magnification. The scale bar is 1 μm. Red circles represent the nanoparticles. (b) The UV–vis–NIR spectra of ALG, CpG, $SP_{II}N$, $TIMmH_{SD}$ solutions. (c) The photos of drug release of $TIMmH_{SD}$ hydrogel from 1.8 mmol/L Ca^{2+} solution at 0, 24 h. (d) The gelation photos of $SP_{II}N$ in Ca^{2+} solution with ALG ($TIMmH_{SD}$) and without ALG ($SP_{II}N$) at different times ([ALG] = 5 mg/mL). The last photo represented the gel status of $TIMmH_{SD}$ after 2 h. (e) The cumulative release of free CpG from the $TIMmH_{SD}$ hydrogel in Ca^{2+} solution which were shaking for one day at 37 °C.

3.2. The evaluation of the photothermal effect

After photoirradiation, the temperatures of ALG had barely changed, while the temperatures of $SP_{II}N$, $TIMmH_S$, $TIMmH_{SD}$ at same concentrations of $SP_{II}N$ had a significantly rising to about 50 °C, proving the well photothermal effect of $SP_{II}N$. And the temperatures of $SP_{II}N$, $TIMmH_S$, $TIMmH_{SD}$ had almost no changes, which showed that ALG and CpG had no effects on the photothermal properties of $SP_{II}N$ (Fig. 3a). In addition, the photothermal capacity of $TIMmH_{SD}$ at different concentrations of $SP_{II}N$ were evaluated and imaged using an infrared thermal imaging camera (Fig. 3b and c). The temperatures of $SP_{II}N$ solutions increased gradually with the increasing of SP_{II} concentration, indicating that SP_{II} had a good concentration dependence. The maximum temperature of $TIMmH_{SD}$ under the NIR-II laser irradiation was up to the 57 °C at about 4 min, which was similar to that of $TIMmH_{SD}$ + laser group. These data showed the similar photothermal effect of both hydrogels (Fig. S5 and Fig. 3d). The temperatures of $TIMmH_S$ and $TIMmH_{SD}$ hydrogel almost unchanged after five heating/cooling cycles, which proved that the $TIMmH_S$ and $TIMmH_{SD}$ hydrogel possessed excellent photothermal stability. Besides, the corresponding thermal photos were imaged in Fig. 3e and f.

3.3. The cytotoxicity and therapeutic efficacy in vitro

To better assess the cytotoxicity and therapeutic efficacy in vitro, the viability of cells was analyzed. The 4T1 cells were cultured with $TIMmH_S$ and $TIMmH_{SD}$ at different $SP_{II}N$ concentrations for one day. Cell viabilities in all groups were over 83%, indicating the well biocompatibility (Fig. 4a). To further investigate the capacity of TIMmH in inhibiting tumor cells, after cocultivation of the 4T1 cells and $TIMmH_S$ and $TIMmH_{SD}$ at various $SP_{II}N$ concentrations for 12 h, the cells were photoirradiated. The results showed that the cells viability of nanoparticles gradually diminished with the increasing $SP_{II}N$ concentrations. At the concentration of 100 μg/mL $SP_{II}N$, the cell viabilities of the 4T1 cells in both $TIMmH_S$ + laser and $TIMmH_{SD}$ + laser were decreased to about 16% (Fig. 4b), revealing the satisfactory TIMmH-produced photothermal effect against tumor cells.

PTT effect was able to activate the ICD procedure, companied by the elevated expression of CRT, as an "eat-me" signal for DC, the increased release of ATP and a non-histone chromatin protein and HMGB-1 from the tumor cells. As such, the three key biomarkers of ICD, including ATP, CRT, and HMGB-1 were analyzed to validate the capacity of TIMmH-induced ICD under the NIR-II photoexcitation in vitro. In the aspects of the release of ATP from 4T1 cells, the ATP level in the $TIMmH_{SD}$ + laser group was 5.38-, 2.56-, 1.08-, 2.80-fold higher than that in the PBS, $TIMmH_S$, $TIMmH_S$ + laser, and $TIMmH_{SD}$ groups (Fig. 4c). As for verifying the expression of CRT, western blot analysis was applied after 12 h of post-treatments. The results indicated that laser irradiation on the both $TIMmH_S$ and $TIMmH_{SD}$ groups effectively enabled the elevation of the expression of CRT on the surface of the 4T1 cells (Fig. 4d). Furthermore, to assess the intratumoral content of the level of HMGB1, the samples in each group were stained and observed. The intratumoral fluorescence intensities of HMGB1 in both $TIMmH_{SD}$ + laser and $TIMmH_S$ + laser groups were relatively lower than that in other groups, which verified that photoirradiation can promote the release of HMGB1 from cells. Owing to the elevated release of HMGB1 from the 4T1 cells, the content of HMGB1 in cells measured in our study was decreased. The above-mentioned results suggested that the TIMmH-mediated photothermal effect was capable of promoting the generation of ICD in vitro (Fig. 4e).

3.4. Evaluation of synergistic thermal immunotherapy in antitumor and anti-metastasis in vivo

The photothermal capacity of $TIMmH_{SD}$ were first evaluated in vivo to verify the effects of PTT. There was no obvious temperature change in the PBS + laser group after photoirradiation, while the temperature changes of the $TIMmH_S$ + laser and $TIMmH_{SD}$ + laser group can rise by more than 20 °C, proving that the prepared hydrogels owned well photothermal conversion capacities in vivo (Fig. S6). After that, encouraged by the excellent photothermal conversion capacities of $TIMmH_{SD}$, the antitumor therapeutic efficacy was further evaluated in the 4T1 tumor-bearing mice. After different treatments, the growths of both primary lesions, distant lesions and lung metastasis were recorded to assess the therapeutic effect (Fig. 5a). The tumor volumes of primary tumors in

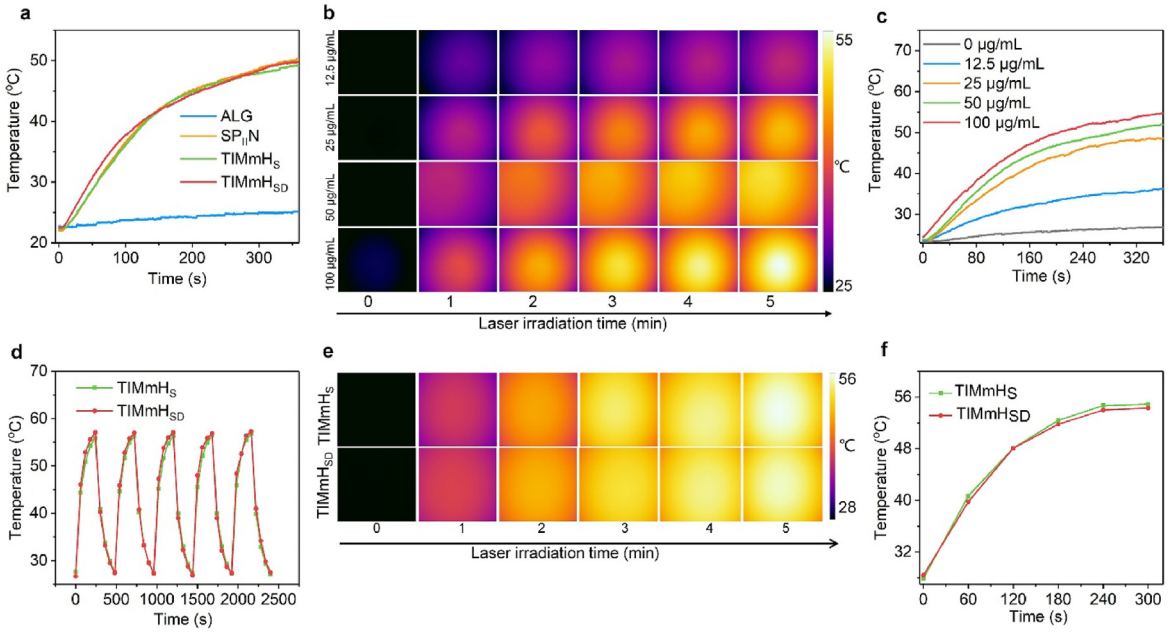

Fig. 3. The evaluation of photothermal property. (a) Photothermal curves of ALG, $SP_{II}N$, $TIMmH_S$, $TIMmH_{SD}$ ($SP_{II}N$ concentration = 100 μg/mL, ALG concentration = 5 mg/mL, CpG concentration = 20 μg/mL) in aqueous solution exposed at 1064 nm laser (1 W/cm^2) for 5 min. (b) The photos of $TIMmH_{SD}$ solution at different concentrations of $SP_{II}N$ under photoirradiation and corresponding the photothermal curves (c). (d) Photothermal stability of $TIMmH_S$ and $TIMmH_{SD}$ hydrogelafter five cycles of laser on/off. (e) The infrared thermal photos of $TIMmH_S$ and $TIMmH_{SD}$ hydrogel under photoirradiation and corresponding the photothermal curves.

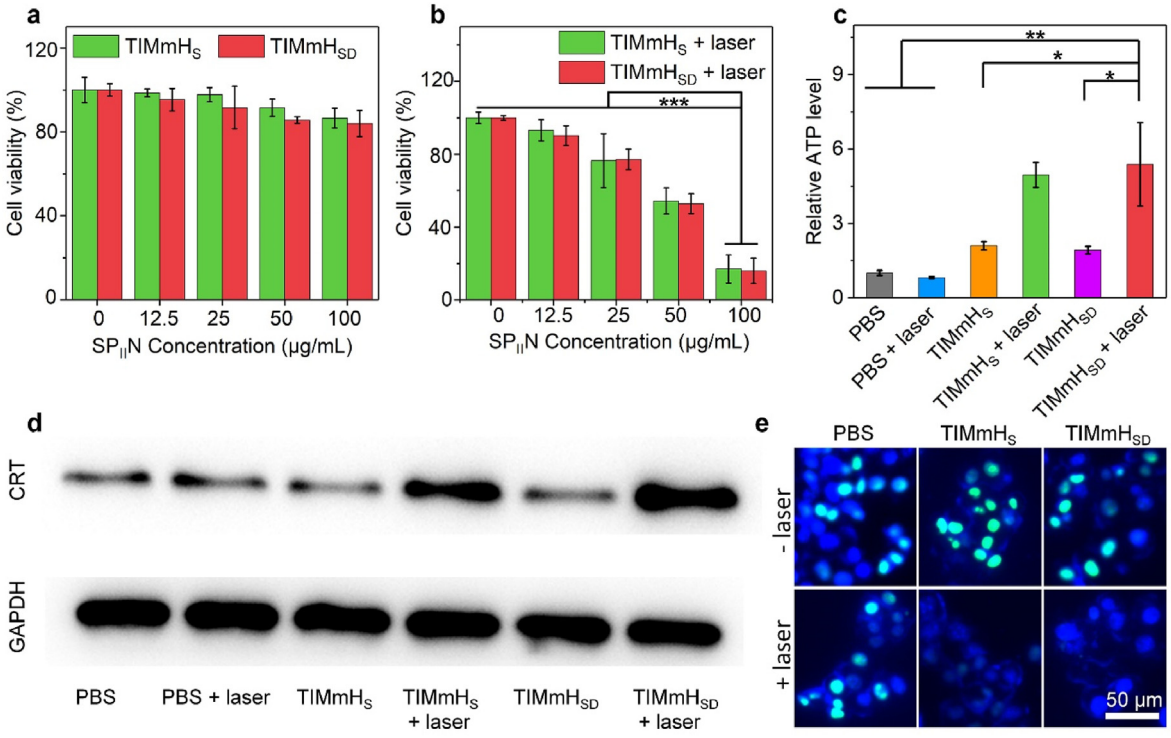

Fig. 4. In vitro treatment of TIMmH$_{SD}$ hydrogel against 4T1 cells and the assess of ICD. (a) The relative cell viability of TIMmH$_S$ and TIMmH$_{SD}$ hydrogel at different concentrations of SP$_{II}$N. (b) The cell viability of TIMmH$_S$ and TIMmH$_{SD}$ hydrogel at different SP$_{II}$N concentrations with 1064 nm laser irradiation (1 W/cm^2, 5min). (c) The relative ATP level in 4T1 with different treatment. (d) The western blot of CRT protein expression in cells from PBS, PBS + laser, TIMmH$_S$, TIMmH$_S$ + laser, TIMmH$_{SD}$ and TIMmH$_{SD}$ + laser group. (e) The fluorescent images of HMGB1 at different groups with or without photoirradiation. The scale bar is 50 μm.

TIMmH$_{SD}$ + laser group was 5.54-, 4.07-, 3.00- and 4.73-fold lower than that in the PBS, TIMmH$_S$, TIMmH$_S$ + laser and TIMmH$_{SD}$ groups, respectively. Similarly, the tumor volumes of distant tumors in TIMmH$_{SD}$ + laser group was also inhibited and was 5.47-, 4.46-, 2.12- and 3.85-fold lower than that in the PBS, TIMmH$_S$, TIMmH$_S$ + laser and TIMmH$_{SD}$ groups, respectively (Fig. 5b and c). Besides, the growth of primary and distant tumors in TIMmH$_S$ + laser and TIMmH$_{SD}$ + laser groups were lower than other groups, which proved that the laser irradiation can suppress tumors growth. And the growth of primary and distant tumors in TIMmH$_{SD}$ + laser group was lower than TIMmH$_{SD}$ + laser group, which shown the drug of CpG also had effect on tumor treatment. As shown in Fig. 5d, the primary and distant of total tumor weights were measured, the tumor weights of TIMmH$_{SD}$ + laser group obtained about 0.42 g, which was 3.81-fold lower than that in the TIMmH$_{SD}$ groups. In addition, the primary and distant tumor inhibition ratio in the TIMmH$_{SD}$ + laser group can reach 88% and 72%, respectively, which was 2.31- and 2.66-fold higher than that in the TIMmH$_{SD}$ respectively (Fig. S7). As the aspect of pathology, the H&E and TUNEL staining of primary tumors in the TIMmH$_{SD}$ + laser represented largest area of cell apoptosis and necrosis compared to other groups. Then, the Ki-67 staining assay also indicated the greatest suppression of malignant cell proliferation in the TIMmH$_{SD}$ + laser group (Fig. 5e). In addition, the survival curve represented that the TIMmH$_S$ + laser and the TIMmH$_{SD}$ + laser groups have longer survival times than other groups (Fig. S8).

In order to further evaluate the anti-metastasis efficiency, after the lung tissue of the different group mice was extracted at 30 days after different treatments. Compared to other groups, no obvious pulmonary metastasis lesions were observed in the TIMmH$_{SD}$ + laser group (Fig. 5f). As depicted in Fig. 5g, the mean number of lung metastasis in TIMmH$_{SD}$ + laser group was 6.72-, 5.57-, 3.57-, and 5.72-fold lower than that in PBS, TIMmH$_S$, TIMmH$_S$ + laser, TIMmH$_{SD}$ groups. These above-mentioned data represented that TIMmH$_{SD}$ was able to repress malignant tumors and prevent tumor metastasis. Moreover, the body weights of mice were recorded every two days to assess the biosafety of the prepared hydrogel. There were almost no changes in the tumor weight of mice in each group (Fig. S9). Additionally, the H&E staining images of heart, liver, spleen, kidney showed no obvious physiological morphology changes (Fig. S10). These results proved that the TIMmH$_{SD}$ hydrogel possessed a good biosafety.

3.5. *Modulating tumor immunosuppressive microenvironment from "cold" to "hot"*

To assess the TIMmH-mediated antitumor immune response induced by combined PTT and CpG-based immunotherapy, the changes of immune cells and cytokines in lymph nodes, tumors, as well as murine serum was analyzed in the treated mice. To further investigate the induction of ICD, the immunofluorescence staining of key molecules was performed. The immunofluorescence staining photos showed the strong green fluorescence signals for CRT and HMGB1 of TIMmH$_{SD}$ + laser and TIMmH$_S$ + laser group in the tumors, indicating elevated expressions of CRT and HMGB1 (Fig. 6a and c). Furthermore, the mean fluorescence intensity (MFI) for CRT in the TIMmH$_{SD}$ + laser group was higher 7.81- and 3.65-fold than PBS and TIMmH$_{SD}$ group, respectively (Fig. 6b). Similarly, as shown in Fig. 6d, the MFI for HMGB1 in the TIMmH$_{SD}$ + laser group was higher 8.40- and 5.43-fold than PBS and TIMmH$_{SD}$ group, respectively. These data proved that TIMmH$_{SD}$-mediated NIR-II thermal effect effectively enabled the production of ICD in vivo. To evaluate the maturation of DCs, the tumor-draining lymph nodes of each treated mouse were extracted and analyzed using flow cytometer assay (Fig. S11). In addition, we further assessed the immune cytokines in murine serum including IL-6, TNF-α, and IFN-γ which are crucial immune cells-released biomarkers in the tumor immunosuppressive microenvironment for modulating T-cell responses. As shown in Fig. 6e–g, the serum levels of IL-6, TNF-α, and IFN-γ in the TIMmH$_{SD}$ + laser group were 1.55-, 1.29-, and 1.45-fold higher than those in the PBS group,

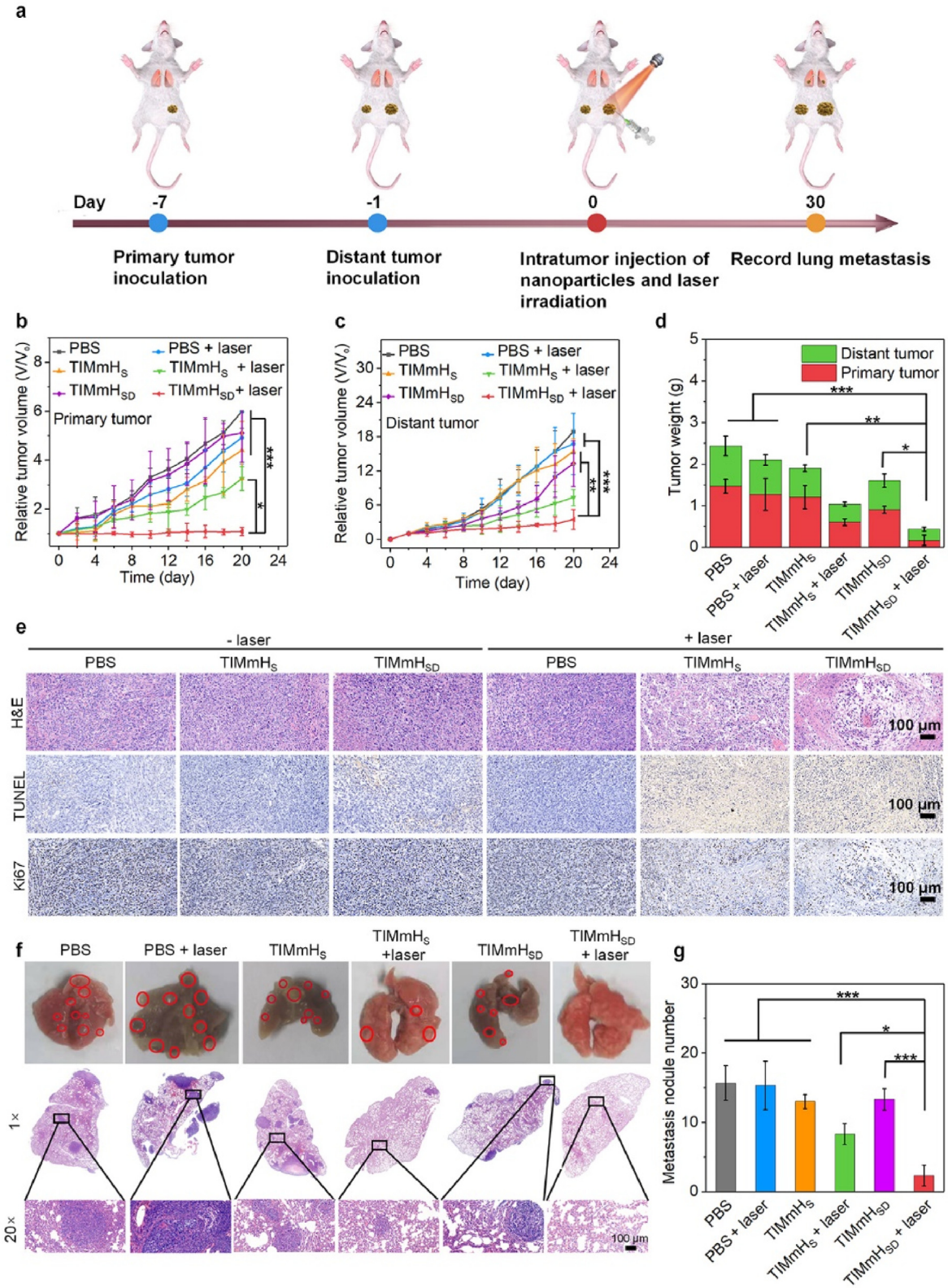

Fig. 5. In vivo synergistic therapeutic effect of $TIMmH_{SD}$ hydrogel. (a) Schematic diagram of the therapeutic experiment. The relative primary tumor volume (b) and distant tumor volume (c) from mice (n = 5) after systemic treatments of PBS, $TIMmH_S$, $TIMmH_{SD}$ (20 μL, $[SP_{II}N]$ = 100 μg/mL, [ALG] = 5 mg/mL, [CpG] = 20 μg/mL) via locally injection with and without 1064 nm laser irradiation (1 W/cm^2, 5 min). (d) The weight of tumors from mice (n = 3). (e) The H&E, TUNEL or Ki67 staining photos of tumor tissue from mice at different treated groups, scale bar = 100 μm. (f) The images of H&E staining and the photos of isolated lung from mice (PBS, PBS + laser, $TIMmH_S$, $TIMmH_S$ + laser, $TIMmH_{SD}$ and $TIMmH_{SD}$ + laser), scale bar = 100 μm. Red circles represent the tumor nodules. (g) The metastasis nodules number in mice at different groups after treatments for 30 days.

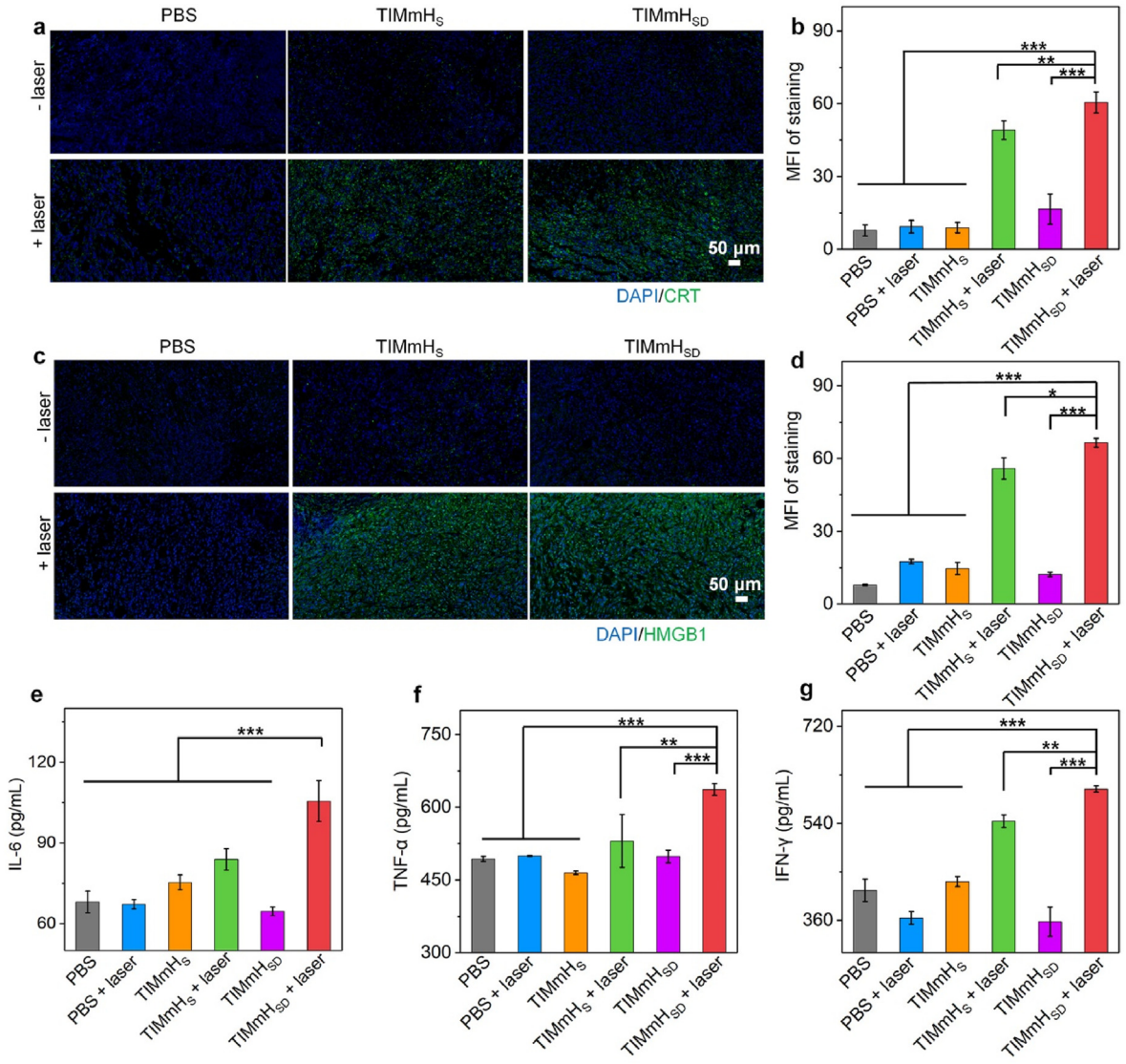

Fig. 6. The effect of ICD and serum level in vivo. (a) The immunofluorescence photos of CRT and corresponding MFI of quantitative data (b). The scale bar is 50 μm. (c) The immunofluorescence photos of HMGB1 tumor tissue from mice and corresponding MFI of quantitative data (d). The scale bar is 50 μm. The blue fluorescence signal indicated cell nucleus stained with DAPI, and green fluorescence signal indicated CRT or HMGB1 stained with antibodies. The serum levels of IL-6 (e), TNF-α (f), and IFN-γ (g) at different treated groups after treatments for three days.

respectively. Additionally, various immune cytokines in tumors were also evaluated. The levels of TNF-α and IFN-γ, and IL-12 (predominant cytokines produced by macrophages) in tumors of TIMmH$_{SD}$ + laser group were 2.09-, 1.36-, 1.41-fold higher than those in the PBS group, and the level of TNF-β in the tumors of TIMmH$_{SD}$ + laser group was 7.55-fold lower than that in the PBS groups (Fig. S12). Moreover, as we know, DCs in the tumor immunosuppressive microenvironment are important in the activation and modulation of the innate and adaptive immunities. As such, we further discovered if TIMmH could stimulate DC maturation in vivo. As shown in Fig. 7a and b, the populations of matured DCs in the tumor-draining lymph nodes (CD11c$^+$CD80$^+$CD86$^+$) of TIMmH$_S$ + laser and TIMmH$_{SD}$ + laser group were 2.1- and 2.4-fold higher than that in the PBS group. Similarly, the populations of matured DCs in the spleen of TIMmH$_S$ + laser and TIMmH$_{SD}$ + laser group were 1.38- and 1.61-fold higher than that in the PBS group (Fig. S13). Notably, the percentages of matured DCs of the tumor-draining lymph nodes and spleen in the TIMmH$_{SD}$ + laser group were 1.29- and 1.17-fold higher than that in the TIMmH$_S$ + laser groups, respectively, showing that the synergic effect of PTT effect and CpG-mediated immunostimulatory action. As for the intratumoral infiltration of T lymphocytes cells including the T helper cells (CD3$^+$CD4$^+$) and CTLs (CD3$^+$CD8$^+$), distant tumors of mice in each group were measured via flow cytometer assay (Fig. S14). Fig. 7c showed that the highest populations of T helper cells and CTLs were observed in TIMmH$_{SD}$ + laser group, which was higher than other groups. The populations of CD3$^+$CD8$^+$ T cells in the TIMmH$_{SD}$ + laser group was up to 15.15%, which was 5.36-, 1.43-, and 3.75-fold higher than that in the PBS, TIMmH$_S$ + laser and TIMmH$_{SD}$ groups, respectively (Fig. 7d). Similarly, the populations of CD3$^+$CD4$^+$ T cells in the TIMmH$_{SD}$ + laser group was 6.27-, 2.12-, and 4.78-fold higher than that in the PBS, TIMmH$_S$ + laser and TIMmH$_{SD}$ groups, respectively (Fig. S15). Moreover, T$_{reg}$, as an important immunosuppressive cell in the tumor microenvironment, was subsequently analyzed. The percentage of T$_{reg}$ (CD25$^+$Foxp3$^+$) in the TIMmH$_{SD}$ + laser group was 2.58-, 1.48-, 2.08-fold lower than that in the PBS, TIMmH$_S$ + laser and TIMmH$_{SD}$ groups, respectively (Fig. S16). These data indicated that the TIMmH strategy could stimulate the T cells immune response and sensitize the immunotherapy of "cold" tumors for modulating the tumor immunosuppressive microenvironment.

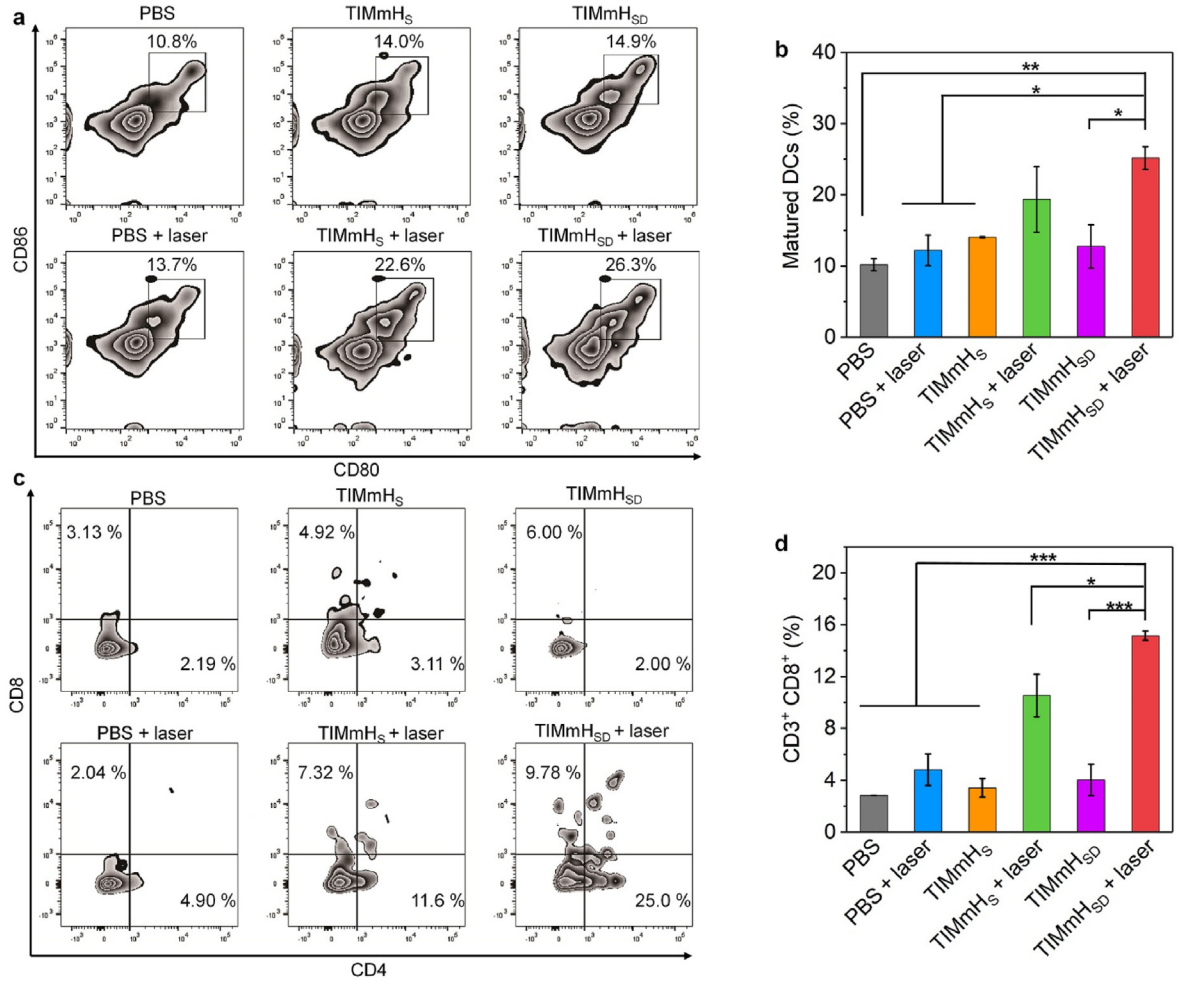

Fig. 7. The evaluation of mature DCs and CD8$^+$ T cell population in vivo. (a) Flow cytometry assay of matured DCs (CD11c$^+$CD80$^+$CD86$^+$) in tumor-draining lymph nodes. (b) Quantitative percentages of matured DCs in tumor-draining lymph nodes. (c) Flow cytometry assay of CD4$^+$ T, CD8$^+$ T cells in distant tumors. (d) Populations of CD3$^+$, CD8$^+$ T cells in distant tumors were extracted from mice at different treatments.

4. Conclusion

In present study, a tumor immunosuppressive microenvironment modulating hydrogel platform was constructed and performed for NIR-II PTT-synergized immunotherapy to acquire the durable inhibition of breast cancer metastasis. Upon the intratumoral administration of ALG solution co-loaded with $SP_{II}N$ and CpG, the TIMmH was in situ formed through Ca^{2+} coordination in the tumor microenvironment, which was contributed to achieving the prolonged accumulation time of drugs and prevention of the premature degradation of CpG. Upon NIR-II photoirradiation, the TIMmH was able to elevate the local temperature for the ablation of tumors, which could efficiently induce the apoptosis of tumor cells, trigger the initiation of tumor ICD and the maturation of DCs. More importantly, such synergistic effect simultaneously enabled the modulation of tumor immunosuppressive microenvironment from "cold" to "hot" immune state. As such, the TIMmH in present study not only served as the excellent vector of immunoadjuvants, but also acquired the thermal immune activation through the modulation of tumor immunosuppressive microenvironment for durable inhibiting the breast tumor growth and lung metastasis. To our knowledge, this study reports the first a tumor immunosuppressive microenvironment modulating hydrogel for breast cancer metastasis-inhibiting treatment. Considering the feasible and easy synthesis of such hydrogel platform, various curable agents (such as gene or immunotherapeutic drugs, etc.) with easy degradation can be loaded into the developed nanohydrogel platform for breast cancer treatment.

Credit author statement

Junjian Shen: Writing – original draft, Investigation, Minghui Lin: Investigation, Resources, Methodology, Mengbin Ding: Software, Formal analysis, Ningyue Yu: Investigation, Methodology, Chun Yang: Resources, Formal analysis, Deping Kong: Data curation, Resources, Haitao Sun: Conceptualization, Validation, Supervision, Writing – review & editing, Zongyu Xie: Validation, Project administration, Writing – review & editing.

Declaration of competing interest

The authors declare that they have no known competing financial interests or personal relationships that could have appeared to influence the work reported in this paper.

Acknowledgements

This study was financially supported by the Medical Empowerment-Pilot Elite Research Project Special Fund (M-HR-YXFN-2021-05-09), The key project of Natural Science Foundation of Education Department of Anhui Province (KJ2019A0402), "Science and Technology Innovation Action Plan" Star Cultivation (Sailing Program) (22YF1443600), and Shanghai Municipal Key Clinical Specialty (shslczdzk03202).

Appendix A. Supplementary data

Supplementary data to this article can be found online at https://doi.org/10.1016/j.mtbio.2022.100416.

References

[1] J.S. O'Donnell, M. Teng, M.J. Smyth, Cancer immunoediting and resistance to T cell-based immunotherapy, Nat. Rev. Clin. Oncol. 16 (3) (2019) 151–167, https://doi.org/10.1038/s41571-018-0142-8.

[2] R.S. Riley, C.H. June, R. Langer, M.J. Mitchell, Delivery technologies for cancer immunotherapy, Nat. Rev. Drug Discov. 18 (3) (2019) 175–196, https://doi.org/10.1038/s41573-018-0006-z.

[3] S. Tan, D. Li, X. Zhu, Cancer immunotherapy: pros, cons and beyond, biomed, Pharmacother 124 (2020), 109821, https://doi.org/10.1016/j.biopha.2020.109821.

[4] T.B. Bertolini, M. Biswas, C. Terhorst, H. Daniell, R.W. Herzog, A.R. Piñeros, Role of orally induced regulatory T cells in immunotherapy and tolerance, Cell, Immunol. 359 (2021), 104251, https://doi.org/10.1016/j.cellimm.2020.104251.

[5] X. He, C. Xu, Immune checkpoint signaling and cancer immunotherapy, Cell Res. 30 (8) (2020) 660–669, https://doi.org/10.1038/s41422-020-0343-4.

[6] M. Saxena, S.H. van der Burg, C. Melief, N. Bhardwaj, Therapeutic cancer vaccines, Nat. Rev. Cancer 21 (6) (2021) 360–378, https://doi.org/10.1038/s41568-021-00346-0.

[7] U. Sahin, Ö. Türeci, Personalized vaccines for cancer immunotherapy, Science 359 (6382) (2018) 1355–1360, https://doi.org/10.1126/science.aar7112.

[8] G. Morad, B.A. Helmink, P. Sharma, J.A. Wargo, Hallmarks of response, resistance, and toxicity to immune checkpoint blockade, Cell 184 (21) (2021) 5309–5337, https://doi.org/10.1016/j.cell.2021.09.020.

[9] S.P. Kubli, T. Berger, D.V. Araujo, L.L. Siu, T.W. Mak, Beyond immune checkpoint blockade: emerging immunological strategies, Nat. Rev. Drug Discov. 20 (12) (2021) 899–919, https://doi.org/10.1038/s41573-021-00155-y.

[10] C.H. June, R.S. O'Connor, O.U. Kawalekar, S. Ghassemi, M.C. Milone, CAR T cell immunotherapy for human cancer, Science 359 (6382) (2018) 1361–1365, https://doi.org/10.1126/science.aar6711.

[11] W. Tomaszewski, L. Sanchez-Perez, T.F. Gajewski, J.H. Sampson, Brain tumor microenvironment and host state: implications for immunotherapy, Clin. Cancer Res. 25 (14) (2019) 4202–4210, https://doi.org/10.1158/1078-0432.CCR-18-1627.

[12] J.A. Joyce, D.T. Fearon, T cell exclusion, immune privilege, and the tumor microenvironment, Science 348 (6230) (2015) 74–80, https://doi.org/10.1126/science.aaa6204.

[13] M. Kostine, A. Finckh, C.O. Bingham, K. Visser, J. Leipe, H. Schulze-Koops, E.H. Choy, K. Benesova, T. Radstake, A.P. Cope, et al., EULAR points to consider for the diagnosis and management of rheumatic immune-related adverse events due to cancer immunotherapy with checkpoint inhibitors, Ann. Rheum. Dis. 80 (1) (2021) 36–48, https://doi.org/10.1136/annrheumdis-2020-217139.

[14] M. Ramos-Casals, J.R. Brahmer, M.K. Callahan, A. Flores-Chávez, N. Keegan, M.A. Khamashta, O. Lambotte, X. Mariette, A. Prat, M.E. Suárez-Almazor, Immune-related adverse events of checkpoint inhibitors, Nat. Rev. Dis. Prim. 6 (1) (2020) 38, https://doi.org/10.1038/s41572-020-0160-6.

[15] Y. Wang, H. Zhang, Y.W. He, The complement receptors C3aR and C5aR are a new class of immune checkpoint receptor in cancer immunotherapy, Front. Immunol. 10 (2019) 1574, https://doi.org/10.3389/fimmu.2019.01574.

[16] Y. Che, Y. Yang, J. Suo, Y. An, X. Wang, Induction of systemic immune responses and reversion of immunosuppression in the tumor microenvironment by a therapeutic vaccine for cervical cancer, Cancer Immunol. Immunother. 69 (12) (2020) 2651–2664, https://doi.org/10.1007/s00262-020-02651-3.

[17] A. Xu, L. Zhang, J. Yuan, F. Babikr, A. Freywald, R. Chibbar, M. Moser, W. Zhang, B. Zhang, Z. Fu, et al., TLR9 agonist enhances radiofrequency ablation-induced CTL responses, leading to the potent inhibition of primary tumor growth and lung metastasis, Cell. Mol. Immunol. 16 (10) (2019) 820–832, https://doi.org/10.1038/s41423-018-0184-y.

[18] S.F. Abdelwahab, S. Hamdy, A.M. Osman, Z.A. Zakaria, I. Galal, M. Sobhy, M. Hashem, W.R. Allam, M. Abdel-Samiee, E. Rewisha, et al., Association of the polymorphism of the Toll-like receptor (TLR)-3 and TLR-9 genes with hepatitis C virus-specific cell-mediated immunity outcomes among Egyptian health-care workers, Clin. Exp. Immunol. 203 (1) (2021) 3–12, https://doi.org/10.1111/cei.13514.

[19] K. Okuya, Y. Tamura, K. Saito, G. Kutomi, T. Torigoe, K. Hirata, N. Sato, Spatiotemporal regulation of heat shock protein 90-chaperoned self-DNA and CpG-oligodeoxynucleotide for type I IFN induction via targeting to static early endosome, J. Immunol. 184 (12) (2010) 7092–7099, https://doi.org/10.4049/jimmunol.1000490.

[20] C. Bode, G. Zhao, F. Steinhagen, T. Kinjo, D.M. Klinman, CpG DNA as a vaccine adjuvant, Expert Rev. Vaccines 10 (4) (2011) 499–511, https://doi.org/10.1586/erv.10.174.

[21] S. Shirai, M. Shibuya, A. Kawai, S. Tamiya, L. Munakata, D. Omata, R. Suzuki, T. Aoshi, Y. Yoshioka, Lipid nanoparticles potentiate CpG-Oligodeoxynucleotide-Based vaccine for influenza virus, Front. Immunol. 10 (2020), https://doi.org/10.3389/fimmu.2019.03018.

[22] L. Munakata, Y. Tanimoto, A. Osa, J. Meng, Y. Haseda, Y. Naito, H. Machiyama, A. Kumanogoh, D. Omata, K. Maruyama, et al., Lipid nanoparticles of Type-A CpG D35 suppress tumor growth by changing tumor immune-microenvironment and activate CD8 T cells in mice, J. Contr. Release 313 (2019) 106–119, https://doi.org/10.1016/j.jconrel.2019.09.011.

[23] C.C. Kuo, C.M. Liang, C.Y. Lai, S.M. Liang, Involvement of heat shock protein (Hsp) 90 beta but not Hsp90 alpha in antiapoptotic effect of CpG-B oligodeoxynucleotide, J. Immunol. 178 (10) (2007) 6100–6108, https://doi.org/10.4049/jimmunol.178.10.6100.

[24] K. Okuya, Y. Tamura, K. Saito, G. Kutomi, T. Torigoe, K. Hirata, N. Sato, Spatiotemporal regulation of heat shock protein 90-chaperoned self-DNA and CpG-oligodeoxynucleotide for type I IFN induction via targeting to static early endosome, J. Immunol. 184 (12) (2010) 7092–7099, https://doi.org/10.4049/jimmunol.1000490.

[25] C. Deng, Q. Zhang, M. Jia, J. Zhao, X. Sun, T. Gong, Z. Zhang, Tumors and their microenvironment Dual-Targeting chemotherapy with local immune adjuvant therapy for effective antitumor immunity against breast cancer, Adv. Sci. 6 (6) (2019), 1801868, https://doi.org/10.1002/advs.201801868.

[26] K.D. Wilson, S.D. de Jong, Y.K. Tam, Lipid-based delivery of CpG oligonucleotides enhances immunotherapeutic efficacy, Adv. Drug Deliv. Rev. 61 (3) (2009) 233–242, https://doi.org/10.1016/j.addr.2008.12.014.

[27] H. Cai, S. Shukla, N.F. Steinmetz, The antitumor efficacy of CpG oligonucleotides is improved by encapsulation in plant virus-like particles, Adv. Funct. Mater. 30 (15) (2020), 1908743, https://doi.org/10.1002/adfm.201908743.

[28] C. Wang, W. Sun, G. Wright, A.Z. Wang, Z. Gu, Inflammation-Triggered cancer immunotherapy by programmed delivery of CpG and Anti-PD1 antibody, Adv. Mater. 28 (40) (2016) 8912–8920, https://doi.org/10.1002/adma.201506312.

[29] H. Sun, T. Yu, X. Li, Y. Lei, J. Li, X. Wang, P. Peng, D. Ni, X. Wang, Y. Luo, Second near-infrared photothermal-amplified immunotherapy using photoactivatable composite nanostimulators, J. Nanobiotechnol. 19 (1) (2021) 433, https://doi.org/10.1186/s12951-021-01197-5.

[30] Y. Zhang, T. Wang, Y. Zhuang, T. He, X. Wu, L. Su, J. Kang, J. Chang, H. Wang, Sodium alginate Hydrogel-Mediated cancer immunotherapy for postoperative in situ recurrence and metastasis, ACS Biomater. Sci. Eng. 7 (12) (2021) 5717–5726, https://doi.org/10.1021/acsbiomaterials.1c01216.

[31] L. Chengnan, Q. Pagneux, A. Voronova, A. Barras, A. Abderrahmani, V. Plaisance, V. Pawlowski, N. Hennuyer, B. Staels, L. Rosselle, et al., Near-infrared light activatable hydrogels for metformin delivery, Nanoscale 11 (34) (2019) 15810–15820, https://doi.org/10.1039/c9nr02707f.

[32] K.Y. Lee, D.J. Mooney, Alginate: properties and biomedical applications, Prog. Polym. Sci. 37 (1) (2012) 106–126, https://doi.org/10.1016/j.progpolymsci.2011.06.003.

[33] D. Zhi, T. Yang, J. O'Hagan, S. Zhang, R.F. Donnelly, Photothermal therapy, J. Contr. Release 325 (2020) 52–71, https://doi.org/10.1016/j.jconrel.2020.06.032.

[34] N. Yu, M. Ding, J. Li, Near-Infrared photoactivatable immunomodulatory nanoparticles for combinational immunotherapy of cancer, Front. Chem. 9 (2021), https://doi.org/10.3389/fchem.2021.701427.

[35] M. Zhan, X. Yu, W. Zhao, Y. Peng, S. Peng, J. Li, L. Lu, Extracellular matrix-degrading STING nanoagonists for mild NIR-II photothermal-augmented chemodynamic-immunotherapy, J. Nanobiotechnol. 20 (1) (2022), https://doi.org/10.1186/s12951-021-01226-3.

[36] X. Li, H. Sun, H. Li, C. Hu, Y. Luo, X. Shi, A. Pich, Multi-responsive biodegradable cationic nanogels for highly efficient treatment of tumors, Adv. Funct. Mater. 31 (26) (2021), 2100227, https://doi.org/10.1002/adfm.202100227.

[37] H. Sun, Q. Zhang, J. Li, S. Peng, X. Wang, R. Cai, Near-infrared photoactivated nanomedicines for photothermal synergistic cancer therapy, Nano Today 37 (2021), 101073, https://doi.org/10.1016/j.nantod.2020.101073.

[38] M. Li, S. Li, H. Zhou, X. Tang, Y. Wu, W. Jiang, Z. Tian, X. Zhou, X. Yang, Y. Wang, Chemotaxis-driven delivery of nano-pathogenoids for complete eradication of tumors post-phototherapy, Nat. Commun. 11 (1) (2020) 1126, https://doi.org/10.1038/s41467-020-14963-0.

[39] X. Dong, J. Liang, A. Yang, Z. Qian, D. Kong, F. Lv, Fluorescence imaging guided CpG nanoparticles-loaded IR820-hydrogel for synergistic photothermal immunotherapy, Biomaterials 209 (2019) 111–125, https://doi.org/10.1016/j.biomaterials.2019.04.024.

[40] S. Yan, X. Zeng, Y. Tang, B.F. Liu, Y. Wang, X. Liu, Activating antitumor immunity and antimetastatic effect through Polydopamine-Encapsulated Core-Shell upconversion nanoparticles, Adv. Mater. 31 (46) (2019), e1905825, https://doi.org/10.1002/adma.201905825.

[41] Z. Li, Y. Hu, Q. Fu, Y. Liu, J. Wang, J. Song, H. Yang, NIR/ROS-responsive black phosphorus QD vesicles as immunoadjuvant carrier for specific cancer photodynamic immunotherapy, Adv. Funct. Mater. 30 (3) (2019), 1905758, https://doi.org/10.1002/adfm.201905758.

[42] J. Ming, J. Zhang, Y. Shi, W. Yang, J. Li, D. Sun, S. Xiang, X. Chen, L. Chen, N. Zheng, A trustworthy CpG nanoplatform for highly safe and efficient cancer photothermal combined immunotherapy, Nanoscale 12 (6) (2020) 3916–3930, https://doi.org/10.1039/c9nr09402d.

[43] J. Li, K. Pu, Semiconducting polymer nanomaterials as Near-Infrared photoactivatable protherapeutics for cancer, Acc. Chem. Res. 53 (4) (2020) 752–762, https://doi.org/10.1021/acs.accounts.9b00569.

[44] J. Li, H. Duan, K. Pu, Nanotransducers for near-infrared photoregulation in biomedicine, Adv. Mater. 31 (33) (2019), 1901607, https://doi.org/10.1002/adma.201901607.
[45] C. Xu, K. Pu, Second near-infrared photothermal materials for combinational nanotheranostics, Chem. Soc. Rev. 50 (2) (2021) 1111–1137, https://doi.org/10.1039/d0cs00664e.
[46] B. Ouyang, F. Liu, S. Ruan, Y. Liu, H. Guo, Z. Cai, X. Yu, Z. Pang, S. Shen, Localized free radicals burst triggered by NIR-II light for augmented low-temperature photothermal therapy, ACS Appl. Mater. Interfaces 11 (42) (2019) 38555–38567, https://doi.org/10.1021/acsami.9b15009.